Supporting Information

Shufan Feng, Lei Wang, Limei Tian, Ying Liu, Ke Hu, Hangxun Xu, Haifeng Wang* and Jianli Hua**

1. Materials

Tetrakis(4-ethynylphenyl)ethene, 2,7-dibromophenazine, $Pd(PPh_3)_2Cl_2$, CuI, DMF, triethylamine and 2,6-dibromoanthracene were purchased from Adamas. Tetrahydrofuran and methanol was purchased from Sinopharm Chemical Reagent Co., Ltd. All chemicals were used directly without further purification.

2. General Characterizations

Powder X-ray diffraction (PXRD) analyses were conducted using the Bruker D8 Advance Powder X-ray Diffractometer. Solid-state ^{13}C-NMR spectra were acquired with the Bruker Advance III 500 MHz spectrometer. Fourier transform infrared (FT-IR) spectra were recorded using KBr pellets on a Nicolet Impact 410 spectrometer. The sample morphology was examined using both a field emission scanning electron microscope (FESEM, JSM-6360LV) and a transmission electron microscope (TEM, JEOL JEM-2100). X-ray photoelectron spectroscopy (XPS) analysis was performed with an ESCALAB 250Xi Thermo Scientific TM XPS equipment. Nitrogen adsorption and desorption at 77 K were carried out using Micromeritics ASAP 2020, with the samples being degassed at 120 °C for 12 hours under a vacuum of 10^{-5} bar prior to analysis. The specific surface areas were calculated using the Brunauer-Emmett-Teller (BET) method, and the pore size distribution was determined from the sorption curve using the non-local density functional theory (NLDFT) model. Diffuse reflectance spectroscopy (DRS) measurements were performed with a Varian Cary 500 spectrophotometer. Electron spin resonance (ESR) spectra were recorded using the Bruker EMX nano instrument. All electrochemical tests were conducted in a standard three-electrode cell using a CHI760E electrochemical workstation. Photoluminescence (PL) spectra were collected using a Hitachi F-4500 fluorescence spectrophotometer. A TSP-2000 (Unisoku) laser flash photolysis system was used to record nanosecond transient absorption spectra.

3. Photocatalytic H_2O_2 Production

In a typical photocatalytic experiment, 5 mg photocatalyst was dispersed in 50 mL of water. Subsequently, the dispersion underwent ultrasonic treatment for 10 minutes, followed by continuous stirring for 30 minutes. All photocatalytic reactions were conducted in an air atmosphere under the illumination of a 300 W xenon lamp, with a UV cut-off filter at 420 nm. At 15-minute intervals, 3 mL of the solution was sampled.

To this solution, 1 mL of 0.1 mol·L^{-1} aqueous potassium hydrogen phthalate ($C_8H_5KO_4$) solution and 1 mL of 0.4 mol·L^{-1} aqueous potassium iodide (KI) solution was added, and the mixture was allowed to sit for 3 hours. Under acidic conditions ($H_2O_2+3I^-+2H^+ \rightarrow I_3^-+2\,H_2O$), H_2O_2 molecules reacted with iodide anions (I^-) to produce triiodide anions (I_3^-) with a strong absorption around 350 nm. The quantity of I_3^- was determined via UV–vis spectroscopy based on the absorbance at 350 nm, which allowed the determination of the amount of H_2O_2 produced during each reaction.

Furthermore, the measurement of apparent quantum efficiency (AQE) for H_2O_2 evolution was conducted under monochromatic light irradiation (300 W xenon lamp, λ = 420, 435, 470, 550, 630 nm) with a 10% filter film. The calculation formula for AQE was estimated as Eq. 1

$$\text{AQE}\ (\%) = \frac{2 \times Number\ of\ evolved\ H_2O_2 molecules}{Number\ of\ incident\ photons} \times 100\ \% = \frac{2 \times C \times NA}{S \times P \times t\frac{\lambda}{h \times c}} \times 100\ \% \quad (1)$$

4. SCC Efficiency Measurements

The solar-to-chemical energy conversion (SCC) efficiency measurement for H_2O_2 evolution was performed under an AM 1.5G solar simulator (100 mW cm^{-2}) equipped with a λ > 420 nm cutoff filter illumination. In an unsealed device comprising a quartz tube, 300 mg of catalysts and 60 ml of water were placed. Throughout the photocatalytic tests, O_2 was continuously bubbled into the container. The SCC efficiency was calculated using the following equation:

$$\text{SCC efficiency}\ (\%) = \frac{\left[\Delta G\ for\ H_2O_2\ generation\ (Jmol^{-1})\right]\left[H_2O_2\ formed\ (mol)\right]}{[Total\ input\ power(W)][Reaction\ time\ (s)]} \times 100\%$$

Where ΔG for H_2O_2 generation is 117 $kJmol^{-1}$ and the irradiated sample areas are 4.0 cm^2 during 1 h of illumination.

5. Rotating disk electrode (RDE) measurements: A glassy carbon rotating disk electrode (PINE Research Instrumentation, USA) served as the substrate for working electrode. The working electrode was prepared as followed: sample (2 mg) were dispersed in EtOH (1 mL) containing Nafion (20 μL) by ultrasonication. The slurry (20 μL) was put onto the disk electrode and dried at room temperature. The linear sweep voltammograms (LSV) were obtained in an O_2-saturated 0.1 M phosphate buffer solution (pH = 7) at room temperature with a scan rate 10 mV s^{-1} and different rotation speeds after O_2 bubbling for 1 hour. During the reaction, light source from the Xe-lamp vertically illuminated at the rotating electrode, where the photoelectrochemical kinetic information and the formation of peroxide could be obtained. The average number of electrons (n) was calculated by Koutecky-Levich equation:

$$\frac{1}{J} = \frac{1}{J_L} + \frac{1}{J_K} = \frac{1}{B\omega^{1/2}} + \frac{1}{J_K}$$

$$B = 0.62nFC_0D_0^{2/3}\nu^{-1/6}$$

where J is the measured current density, J_K and J_L are the kinetic and diffusion-limiting current densities, ω is the angular velocity, n is transferred electron number, F is Faraday constant (96485 C mol^{-1}), C_0 is the bulk concentration of O_2 (1.26×10^{-6} mol cm^{-3}), D_0 is the diffusion coefficient of O_2 in 0.1 M phosphate buffer solution (2.7×10^{-5} cm^2 s^{-1}), and ν is kinetic viscosity of the electrolyte (0.01 cm^2 s^{-1}), respectively.

6. *In situ* diffuse reflectance infrared Fourier transform spectroscopy measurements

In situ diffuse reflectance infrared Fourier transform spectroscopy (DRIFTS) measurements were performed using a Bruker IFS 66v Fourier-transform spectrometer equipped with a Harrick diffuse reflectance accessory at the Infrared Spectroscopy and Microspectroscopy Endstation (BL01B) in National Synchrotron Radiation Laboratory (NSRL), Hefei. After Ar gas sweeps the sample for 30 min, vapor and Ar were purged into the reactor with a 300W xenon lamp (> 420nm) used to illuminate the sample.

7. Computational details

The spin-polarized calculations were conducted using Perdew-Burke-Ernzerhof (PBE) functional and generalized gradient approximation (GGA) exchange[1] method within the framework of plan-wave pseudo-potential DFT method, implemented in the

Vienna Ab Initio Simulation Package (VASP) code.[2,3] The project-augmented wave (PAW)[4] method was utilized to represent the core-valence electron interaction, and the valance electronic states were expanded in plane wave basis set with the energy cutoff of 450 eV.[5] The relaxation of all ionic degrees of freedom employed the Broyden-Fletcher-Goldfarb-Shanno (BFGS) algorithm until the Hellman-Feynman forces on each ion were reduced to less than 0.05 eV/Å.[6-8] The transition states were searched using a constrained optimization scheme, and were verified when (i) all forces on atoms vanish; and (ii) the total energy is a maximum along the reaction coordinate but a minimum with respect to the rest of the degrees of freedom. The HOMO and LOMO based on density functional theory (DFT) with GGA were calculated to analyse electron trapping capacity.

The catalyst structures were constructed in a supercell with the lattice a = 30 Å, b = 30 Å, c= 30 Å for TPE-PNZ, PY-PNZ and TPE-AC and a = 25 Å, b = 25 Å, c= 15 Å for BZ-PNZ. A corresponding (1×1×1) k-point mesh was used for all structural optimization and all atoms were allowed to relax.

The adsorption energy of X species ($E_{ads(X)}$) is defined as follows:

$$E_{ads}(X) = E_{total} - E_{catal} - E_X$$

where E_{catal}, E_X and E_{total} are the energies for the clean catalysts, X species in the gas phase and X species adsorbed on the catalysts, respectively. The more negative the $E_{ads}(X)$ is, the stronger species X binds on the catalysts.

8. Synthesis of the CMPs

8.1 Synthesis of TPE-PNZ

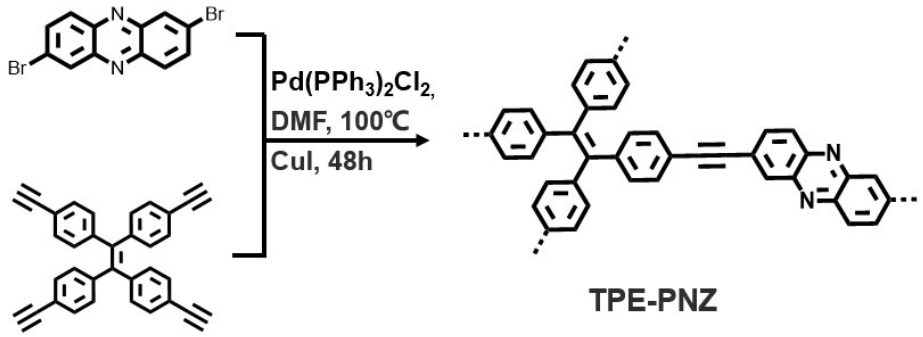

Figure S1. Synthesis of TPE-PNZ

In a 500 mL round-bottom flask, tetrakis(4-ethynylphenyl)ethene (128 mg, 0.3 mmol) and 2,7-dibromophenazine (201 mg, 0.3 mmol) were placed along with $Pd(PPh_3)_2Cl_2$ (20 mg, 0.03 mmol), CuI (10 mg, 0.05 mmol), DMF (15 mL), and triethylamine (15 mL). The mixture underwent degassing with argon for 10 minutes. The flask was then stirred at 100 °C for 48 hours under an argon atmosphere. The resulting precipitate was gathered by filtration and subjected to successive Soxhlet extraction with tetrahydrofuran (24 hours) and methanol (24 hours) to eliminate any remaining unreacted precursors. The final solid sample was dried under vacuum at 60°C for a duration of 12 hours. (340 mg, 78% yield).

8.2 Synthesis of TPE-AC

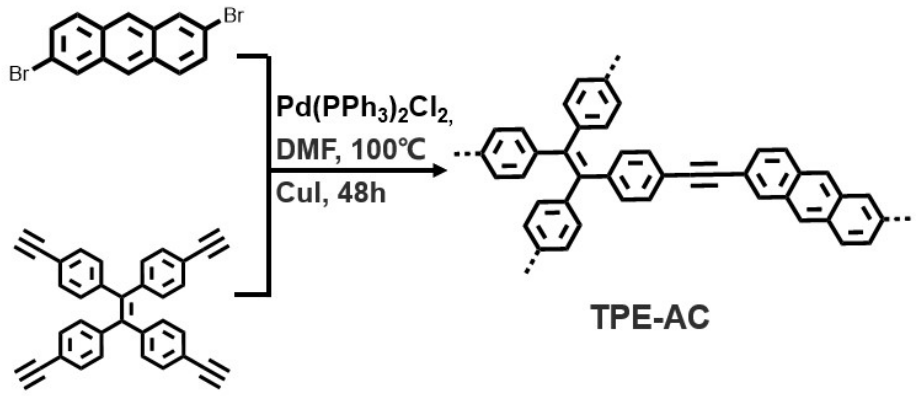

Figure S2. Synthesis of TPE-AC

In a 500 mL round-bottom flask, tetrakis(4-ethynylphenyl)ethene (128 mg, 0.3 mmol) and 2,6-dibromoanthracene (201 mg, 0.6mmol) were placed along with

$Pd(PPh_3)_2Cl_2$ (20 mg, 0.03 mmol), CuI (10 mg, 0.05 mmol), DMF (15 mL), and triethylamine (15 mL). The mixture underwent degassing with argon for 10 minutes. The flask was then stirred at 100 °C for 48 hours under an argon atmosphere. The resulting precipitate was gathered by filtration and subjected to successive Soxhlet extraction with tetrahydrofuran (24 hours) and methanol (24 hours) to eliminate any remaining unreacted precursors. The final solid sample was dried under vacuum at 60°C for a duration of 12 hours. (157 mg, 80% yield).

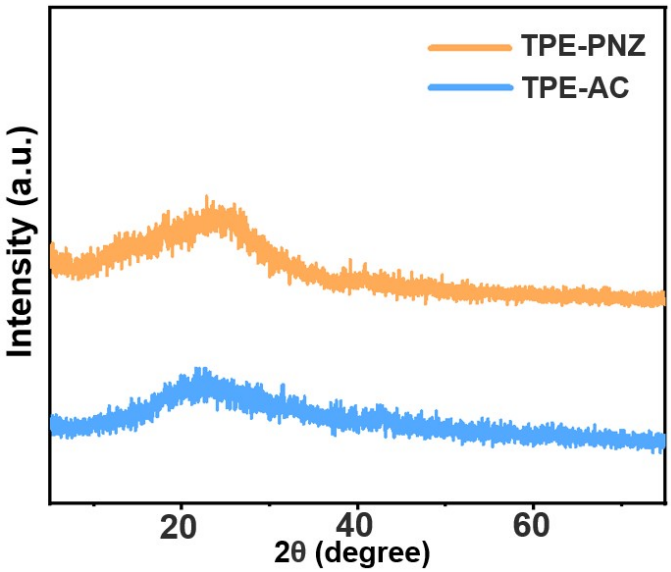

Figure S3. The PXRD patterns of as-synthesized CMPs.

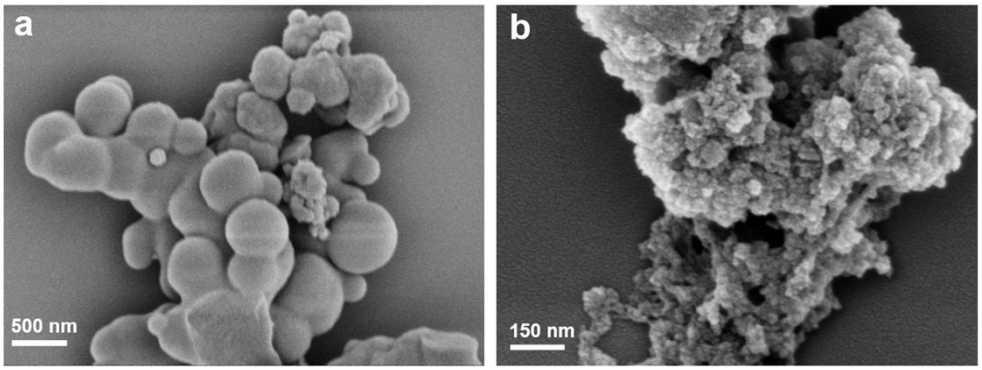

Figure S4. SEM images of (a) TPE-PNZ and (b) TPE-AC.

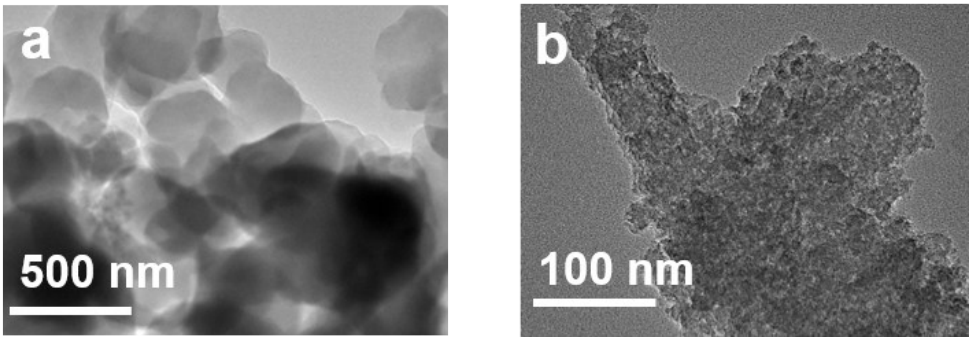

Figure S5. TEM images of (a) TPE-PNZ and (b) TPE-AC.

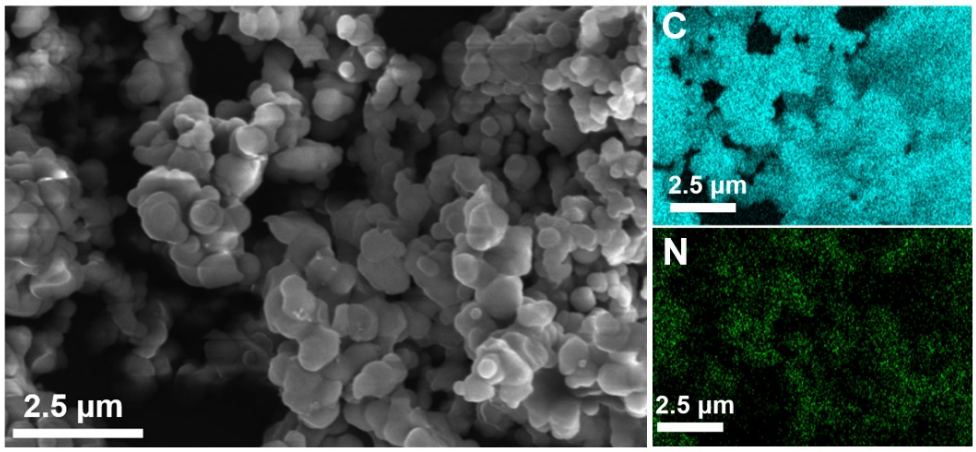

Figure S6. EDX mapping images of TPE-PNZ.

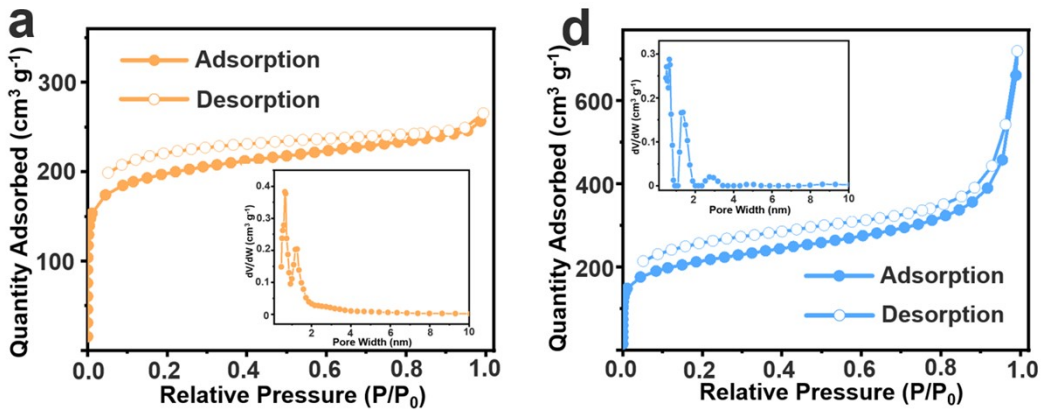

Figure S7. Nitrogen adsorption/desorption isotherms of (a) TPE-PNZ and (b) TPE-AC. Insets show pore size distributions calculated from the nonlocal density functional theory model.

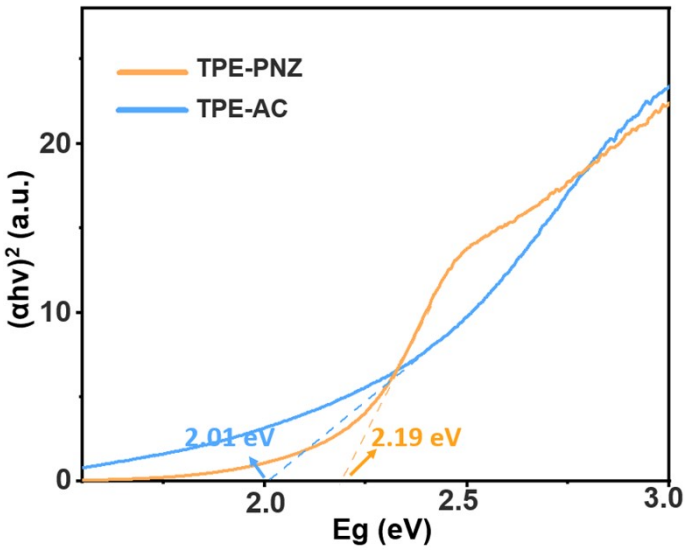

Figure S8. Tauc plots of both CMPs.

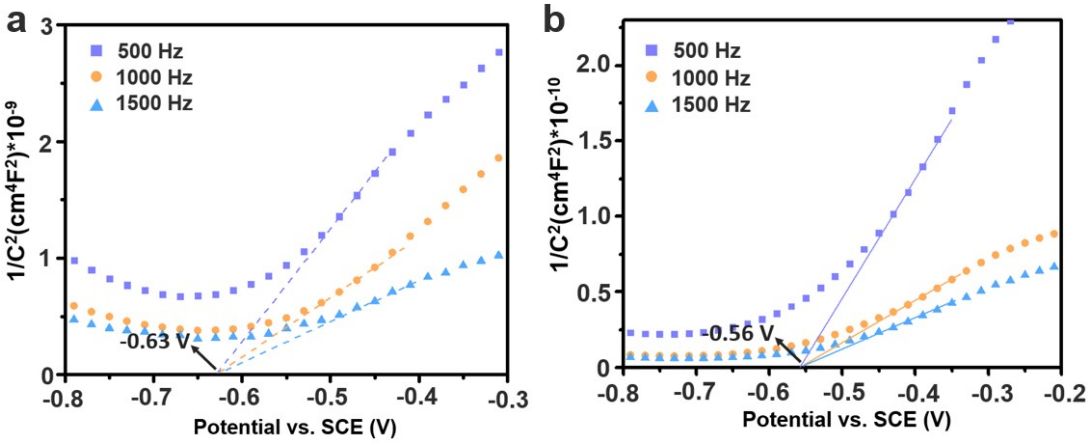

Figure S9. Mott-Schottky plots of (a) TPE-PNZ and (b) TPE-AC.

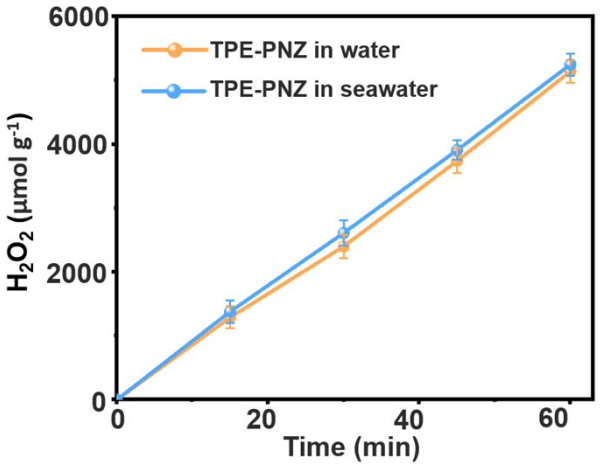

Figure S10. Photocatalytic performances of TPE-PNZ in water and seawater. Error bars are derived from standard errors from three tests.

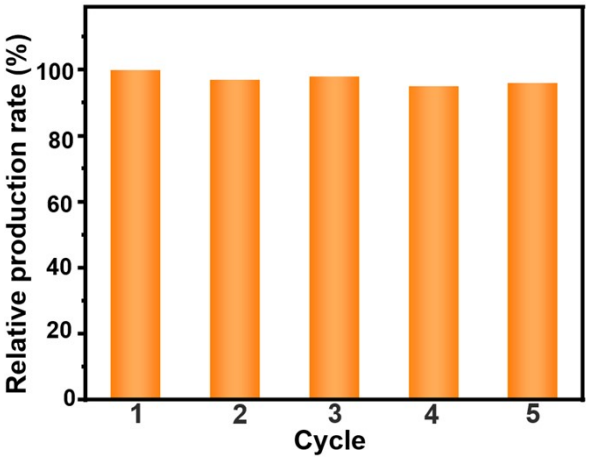

Figure S11. Cycling performance of TPE-PNZ.

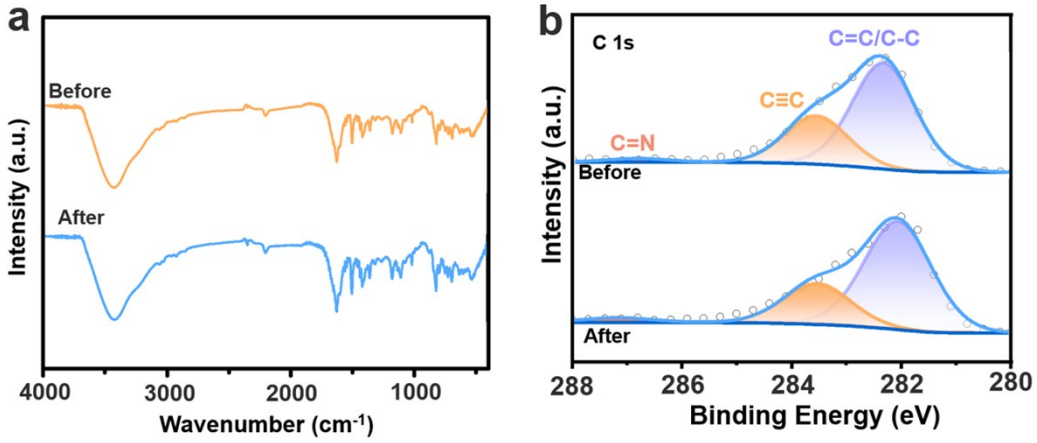

Figure S12. FITR and high-resolution of N *1s* XPS spectra of TPE-PNZ before and after photocatalytic reaction.

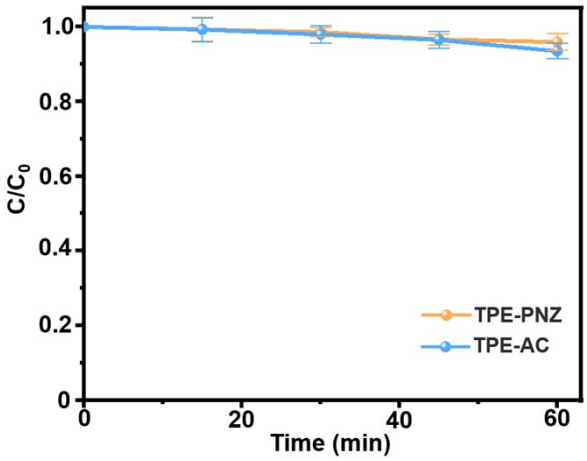

Figure S13. Photocatalytic decomposition of H_2O_2 in pure water by TPE-PNZ and TPE-AC.

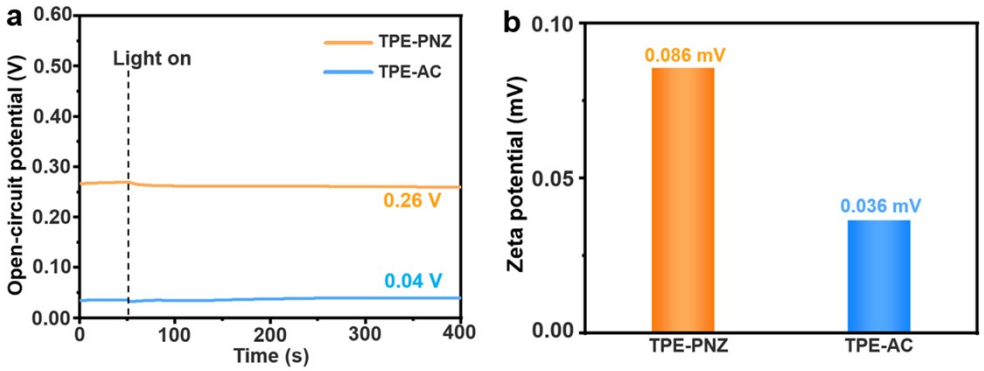

Figure S14. (a) The open circuit potentials and (b) zeta potentials of TPE-PNZ and TPE-AC.

The literature reports that the built-in electric field magnitude can be measured using the formula reported by Kanata et al.

$Fs = (-2V_s\rho/\varepsilon\varepsilon_0)^{1/2}$

Where Fs is the internal electric field magnitude, V_s is the surface potential, ρ is the surface charge density, Ɛ is the low-frequency dielectric constant, and $Ɛ_0$ is the vacuum dielectric constant. The above equation suggests that the in electric field magnitude is mainly determined by the surface voltage and the surface charge density since Ɛ and $Ɛ_0$ are two constants.[9]

Surface voltage can be characterized by open circuit potential. The surface voltage of TPE-PNZ and TPE-AC is 0.26 V and 0.04 V, respectively. Surface charge density can be measured by zeta potential, which is 0.086 and 0.036 mV for TPE-PNZ and TPE-AC, respectively.

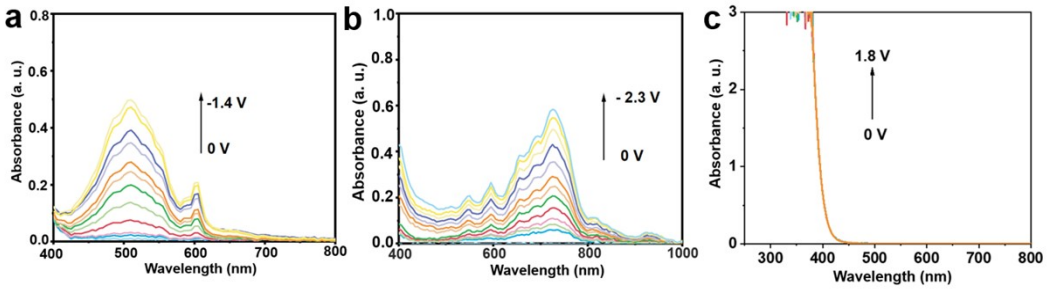

Figure S15. Spectroelectrochemical spectra of (a) phenazine (b) anthracene and (c) tetraphenylethylene.

Using the spectroelectrochemical method, increasing voltage results in the emergence of characteristic peaks for phenazine radical anion ($PNZ^{\bullet-}$) and anthracene radical anion ($AC^{\bullet-}$) at 500 nm (Figures S15a and b). Simultaneously, the spectra of the TPE donor showed no absorption of tetraphenylethylene radical cation ($TPE^{\bullet+}$) at 500 nm (Figure S15c), meaning that the peak of TPE^{+} at 500 nm does not interfere with $PNZ^{\bullet-}$ and $AC^{\bullet-}$. Therefore, it can be inferred that the absorption at 500 nm following the excitation of CMPs can be attributed to the formation of two charge-separated states ($TPE^{\bullet+}$-$PNZ^{\bullet-}$ and $TPE^{\bullet+}$-$AC^{\bullet-}$).

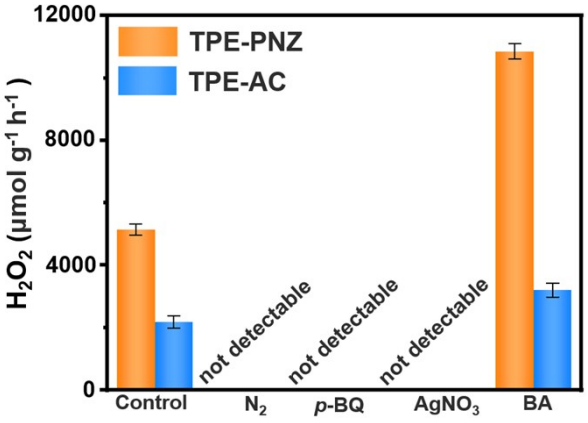

Figure S16. Comparison of H_2O_2 production by TPE-PNZ and TPE-AC under different conditions.

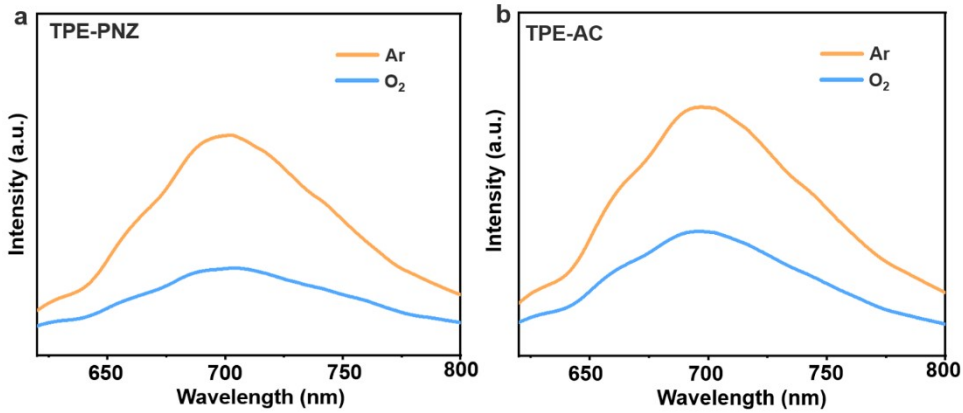

Figure S17. Fluorescence spectra of (a) TPE-PNZ and (b) TPE-AC under Ar and O_2 atmospheres.

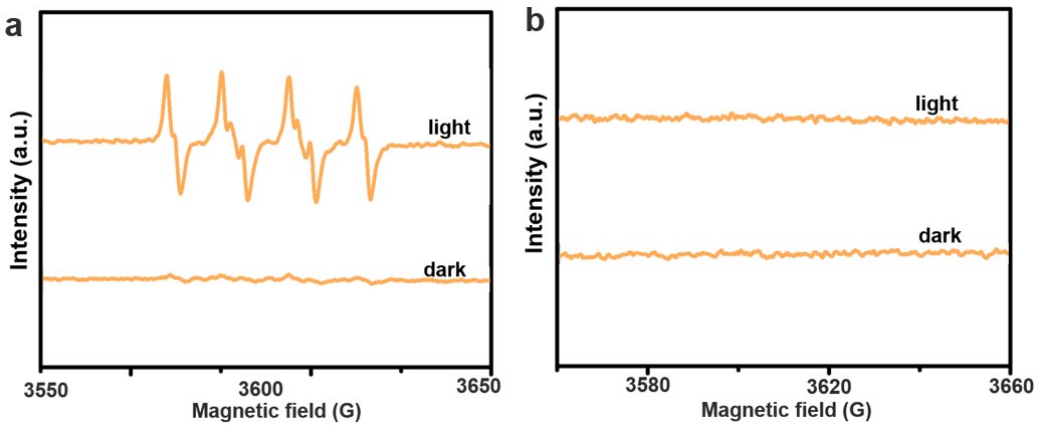

Figure S18. (a) EPR spectra of TPE-PNZ in dark and light irradiation in water/methanol (9/1: v/v) under O_2 atmosphere. (b) EPR spectra of TPE-PNZ in dark and irradiation in $AgNO_3$ aqueous solutions under Ar atmosphere.

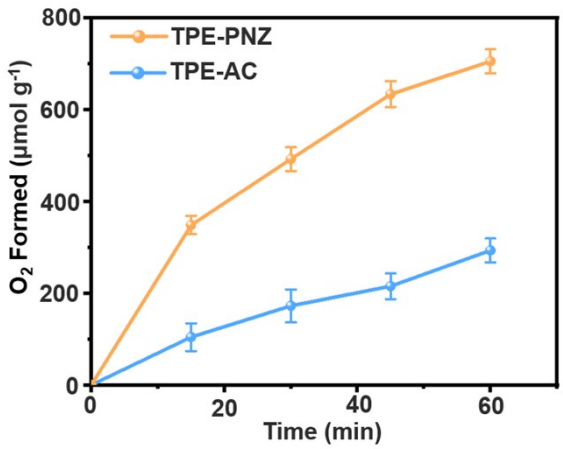

Figure S19. Time-dependent formation of O_2 in $AgNO_3$ aqueous solutions. Error bars are derived from standard errors from three tests.

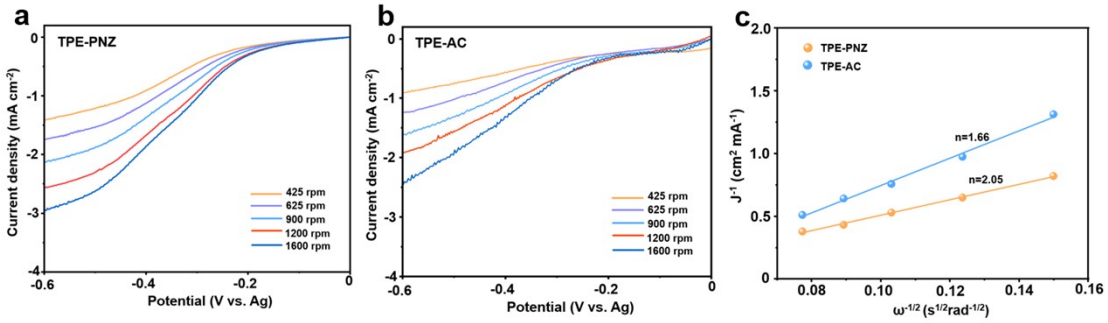

Figure S20. Linear-sweep RDE voltammograms of (a) TPE-PNZ and (b) TPE-AC. (c) The Koutecky-Levich plots obtained by RDE measurements at -0.5 V (versus Ag/AgCl).

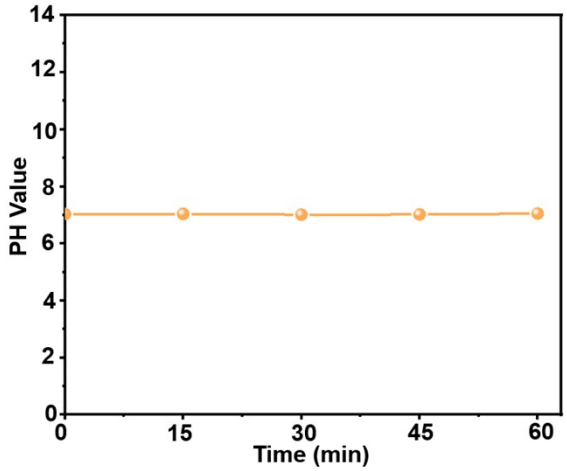

Figure S21. Changes in pH value over photocatalytic time

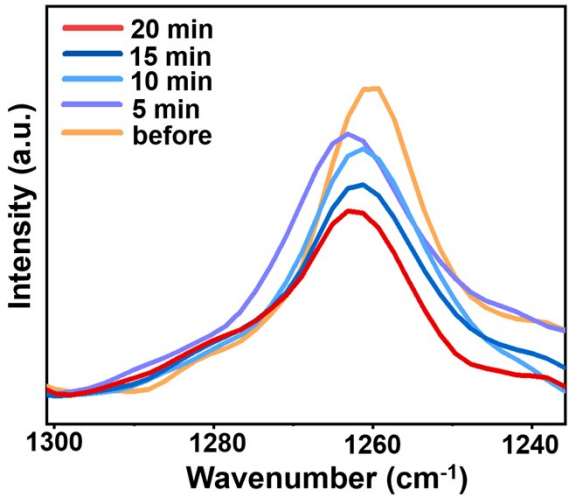

Figure S22. Overlaid *in-situ* DRIFTS of TPE-PNZ saturated with Ar under visible light irradiation

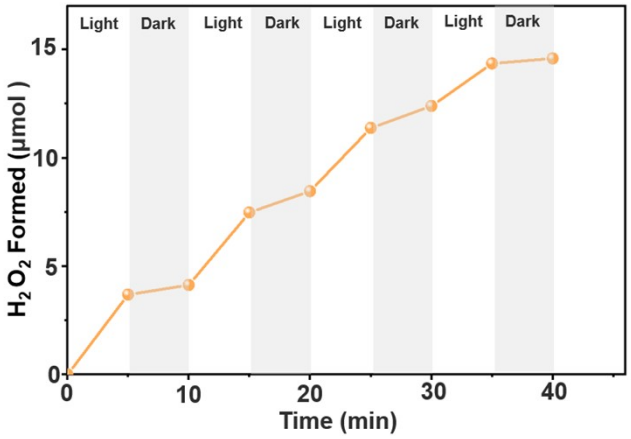

Figure S23. Light and dark processes measured using TPE-PNZ.

Table S1. Summary of recently reported H_2O_2 production rates and SCC efficiencies by different CMPs.

Photocatalysts	Conditions	H_2O_2 yield rate ($\mu mol\ g^{-1}\ h^{-1}$)	SCC (%)	Ref.
TPE-PNZ	**air, H_2O; λ≥420 nm**	**5142**	**0.58**	**This work**
TPE-AQ	air, H_2O; λ≥400 nm	909	0.26	[10]
TPT-alkynyl-AQ	air, H_2O; λ≥400 nm	2368	0.35	[11]
Furan-BILP	O_2, H_2O; λ≥420 nm	2200	-	[12]
AQTEE-COP	O_2, H_2O; λ≥400 nm	3204	-	[13]
P-TAME	O_2, H_2O; λ≥420 nm	1000	-	[14]
Th-CMP	O_2, H_2O; λ≥400 nm	1710	0.17	[15]
PBNCZ-COO$^-$	O_2, H_2O; λ≥420 nm	1719.03	-	[16]
CQD-CTFs	O_2, H_2O; λ≥420 nm	1036	0.21	[17]
PAF-363	O_2, H_2O; λ≥420 nm	3930		[18]
CMP	O_2, H_2O; 300W Xenon lamp	3681.45		[19]
AQTT-COP	O_2, H_2O; λ≥400 nm	3221		[20]
TCFPP-TPD	O_2, H_2O; λ≥420 nm	1180	0.25	[21]
Bpt-CTF	O_2, H_2O; 300W Xenon lamp	3268.1		[22]
CTTP	O_2, H_2O; AM=1.5	1858		[23]
CTP-TD	O_2, H_2O; λ≥420 nm	1342		[24]
CTF-LTZ	O_2, H_2O:EtOH (9:1); 300W Xenon lamp	4068		[25]

Table S2. The comparison of Pd contents and H_2O_2 production performances between TPE-PNZ and TPE-AC.

	TPE-PNZ	**TPE-AC**
Pd content (%)	0.74	0.84
H_2O_2 production rates (μmol h^{-1} g^{-1})	5142	2183

References:

[1] J. Perdew, A. Ruzsinszky, G. Csonka, O, Phys. *Rev. Lett.* **2008**, *100*, 136406

[2] G. Kresse, J. Hafner, *Phys. Rev. B* **1994**, *49*, 14251–14269.

[3] Kresse, G, Furthmüller, *Comp. Mater. Sci.* **1996**, *6*, 15–50.

[4] M. Payne, M. P. Teter, D. C. Allan, T. Arias, J. Joannopoulos, *Rev. Mod. Phys.* **1992**, *64*, 1045.

[5] G. Kresse, D. Joubert, *Phys. Rev. B* **1999**, *59*, 1758–1775.

[6] Y. Dai, Math. *Program*. **2013**, *138*, 501–530

[7] D. Wang, H. Wang, P. Hu, *Physical Chem. Phys*. **2015**, 17, 1549–1555.

[8] J. Zhang, C. Peng, H. Wang, P. Hu, *ACS Catal*. **2017**, 7, 2374–2380.

[9] J. Jing, J. Yang, Z. Zhang, Y. Zhu, *Adv. Energy Mater.* **2021**, 2101392.

[10] Y.-X. Ye, J. Pan, Y. Shen, M. Shen, H. Yan, J. He, X. Yang, F. Zhu, J. Xu, J. He, G. Ouyang, *Proc. Natl. Acad. Sci. U.S.A.* **2021**, 118, e2115666118.

[11] H. Yan, M. Shen, Y. Shen, X.-D. Wang, W. Lin, J. Pan, J. He, Y.-X. Ye, X. Yang, F. Zhu, J. Xu, J. He, G. Ouyang, *Proc. Natl. Acad. Sci. U.S.A.* **2022**, 119, e2202913119.

[12] T. Yang, Y. Jin, Y. Wang, A. Kong, Y. Chen, Y. Zou, C. Liu, G. Wei, C. Yu, *Adv. Funct. Mater*. **2023**, 33, 2300714.

[13] X. Xu, R. Sa, W. Huang, Y. Sui, W. Chen, G. Zhou, X. Li, Y. Li, H. Zhong, *ACS Catal*. **2022**, 12, 12954–12963.

[14] Z. Luo, X. Chen, Y. Hu, X. Chen, W. Lin, X. Wu, X. Wang, *Angew. Chem. Int.*

Ed. **2023**, *62*, e202304875.

[15] T. Gao, C. Yang, Y. Zheng, Y. Shen, Q. Wang, L. Wang, R. Xu, M. Lv, M. Li, Z. Shi, L. Wang, X. Y. Kong, L. Ye, *Appl. Catal. B Environ.* **2024**, *346*, 123761.

[16] X. Xia, J. Feng, Z. Zhong, X. Yang, N. Li, D. Chen, Y. Li, Q. Xu, J. Lu, *Adv. Funct. Mater.* **2023**, 202311987.

[17] Y. Yang, Q. Guo, Q. Li, L. Guo, H. Chu, L. Liao, X. Wang, Z. Li, W. Zhou, *Adv. Funct. Mater.* **2024**, 2400612.

[18] L. Cao, C. Wang, H. Wang, X. Xu, X. Tao, H. Tan, G. Zhu, *Angew. Chem. Int. Ed.* **2024**, e202402095.

[19] X. Li, G. Zhang, N. Li, Q. Xu, H. Li, J. Lu, D. Chen, *Adv. Funct. Mater.* **2024**, 2316773.

[20] X. Xu, Y. Sui, W. Chen, G. Zhou, Y. Li, H. Zhong, H.-R. Wen, *ACS Appl. Polym. Mater.* **2023**, *5*, 7571–7580.

[21] R. Zhang, H. Zhao, C. Pan, J. Zhang, L. Jian, X. Sun, R. Ji, J. Li, Y. Dong, Y. Zhu, *New J. Chem.* **2024**, *48*, 3316–3324.

[22] C. Wu, Z. Teng, C. Yang, F. Chen, H. B. Yang, L. Wang, H. Xu, B. Liu, G. Zheng, Q. Han, *Adv. Mater.* **2022**, *34*, 2110266.

[23] Y. Guo, Y. Dong, B. Liu, B. Ni, C. Pan, J. Zhang, H. Zhao, G. Wang, Y. Zhu, *Adv. Funct. Mater.* **2024**, 2402920.

[24] Q. Zhang, J. Zhou, H. Zhang, C. Qi, Q. Zhou, R. Guo, H. Yang, T. Xing, M. Wang, M. Wu, W. Wu, *Adv. Funct. Mater.* **2024**, 2401579.

[25] P. Gao, C. Wu, S. Wang, G. Zheng, Q. Han, *J. Colloid Interface Sci.* **2023**, *650*, 40–46.